THEMIS observations and modeling of multiple ion species and EMIC waves: Implications for a vanishing He^+ stop band

Justin H. Lee,[1,2] Lunjin Chen,[3] Vassilis Angelopoulos,[1] and Richard M. Thorne[3]

Received 18 January 2012; revised 22 March 2012; accepted 26 April 2012; published 5 June 2012.

[1] Observations of left-hand polarized electro-magnetic ion cyclotron (EMIC) waves with significant wave power across f_{He+} are presented. Concurrent field and particle measurements reveal pitch angle scattering of thermal ions during the interval of maximum wave power. The observations suggest the presence of multiple cold ion species (H^+, He^+) at this time, below the sum of spacecraft potential and minimum energy of the ion instrument (i.e., $<\sim$20 eV). Fortuitously, immediately following the most intense wave activity, the ambient plasma flow velocity became sufficiently large such that cold ions can be accelerated into the energy range of the particle instrument. Thus, two low energy ion components are revealed in the particle measurements at energies consistent with cold protons and He^+. Maxwellian fits provide approximations of these cold ion species component densities and temperatures. The linear dispersion relation of parallel propagating EMIC waves for the observed conditions shows a vanishing cold plasma He^+ stop band, consistent with the wave measurements during this interval. These results provide the first observational evidence of the importance of the cool ion species temperature/density in controlling linear wave growth through the heavy ion stop bands in warm plasma theory.

Citation: Lee, J. H., L. Chen, V. Angelopoulos, and R. M. Thorne (2012), THEMIS observations and modeling of multiple ion species and EMIC waves: Implications for a vanishing He^+ stop band, *J. Geophys. Res.*, *117*, A06204, doi:10.1029/2012JA017539.

1. Introduction

[2] Space-based observations of electro-magnetic ion cyclotron (EMIC) waves have revealed a number of defining features of the low-frequency plasma emissions that match those determined through extensive theoretical work. These left-hand polarized waves experience excitation through cyclotron resonance with anisotropic energetic protons near the magnetic equator and often emit power in separate frequency bands, usually with clear band gaps or "stop bands" at the local gyrofrequencies of He^+ and O^+. Past case studies that combine spacecraft data sets and theory have focused on the processes through which the wave emissions are excited and the characteristics of multiple plasma species that support or suppress this excitation [e.g., *Mauk and McPherron*, 1980; *Young et al.*, 1981; *Roux et al.*, 1982]. The likelihood of the waves leading to losses of high-energy electrons [*Thorne and Kennel*, 1971] has also seen some recent experimental investigation [e.g., *Meredith et al.*, 2003]. The role of He^+ in the generation of EMIC waves has received special attention since the waves tend to possess more power below the He^+ gyrofrequency (f_{He+}) [*Chen et al.*, 2009; *Fraser et al.*, 2010]. Furthermore, the recent observational evidence of waves near the heavy ion gyrofrequency and even throughout the cold plasma theory He^+ stop band suggests that the minimum resonant energy for wave-particle interaction by anomalous Doppler-shift with high-energy electrons is very much reduced [*Ukhorskiy et al.*, 2010], rendering these waves an important candidate for relativistic electron losses. Thus, it is important to understand the origin of and establish the conditions for the growth of EMIC waves near and inside the He^+ stop band.

[3] Recently, test particle simulations within a simplified magnetic field model have adequately reproduced spacecraft observations of simultaneous EMIC wave emissions in two separate frequency bands [*Shoji and Omura*, 2011; *Shoji et al.*, 2011]. These hybrid simulations demonstrate the complicated processes that link cyclotron resonance to wave instability in different frequency bands. At the same time, analytical solutions of the waves as the model plasma environment is modified have been discussed by *Silin et al.* [2011] and *Chen et al.* [2011]. These studies suggest that the cold plasma approximation does not adequately describe the wave characteristics as the wave dispersion and unstable frequencies are modified substantially near f_{He+} by the hot proton anisotropy and cold heavy ion temperature and density.

[1]Institute of Geophysics and Planetary Physics, University of California, Los Angeles, California, USA.
[2]Also at The Aerospace Corporation, Los Angeles, California, USA.
[3]Department of Atmospheric and Oceanic Sciences, University of California, Los Angeles, California, USA.

Corresponding author: J. H. Lee, Institute of Geophysics and Planetary Physics, University of California, 3845 Slichter Hall, 603 Charles E. Young Dr. E., Los Angeles, CA 90095-1567, USA. (justin.h.lee@aero.org)

0148-0227/12/2012JA017539

Additionally, the studies focus on how this dispersion relation modification affects evaluation of electron scattering energies associated with EMIC waves; it is shown that using the cold plasma description of EMIC waves can result in erroneous estimates of the minimum resonant energy of electrons. *Chen et al.* [2011] concluded that the class of EMIC waves which do not have a cold He^+ stop band can only resonate with electrons>a few MeV due to catastrophic damping that occurs at larger wave number. Furthermore, they demonstrate that even when there is a He^+ stop band, the effects of finite He^+ and hot proton temperature can significantly alter the wave properties at frequencies just under Ω_{He+}, also limiting the range of electron energies that can be affected by EMIC waves to much higher energies; sub-MeV electrons cannot be scattered by such waves. Their conclusions imply that the multi-ion species in the plasma environment must be considered more closely when evaluating relativistic electron scattering by EMIC waves. The theoretical predictions still await testing to new, high-resolution observational data.

[4] Such studies continue to improve definition and provide additional understanding of EMIC waves and the various conditions of the plasma environment that excite or damp them. In recent years, a number of observational studies on interactions of various electro-magnetic waves and particles in the equatorial magnetosphere fueled by the launch of the Time History of Events and Macroscale Interactions during Substorms (THEMIS) mission have also been carried out using state-of-the-art, comprehensive instrumentation [e.g., *Usanova et al.*, 2008; *Li et al.*, 2010]. In particular, burst-mode observations (particle and wave data captures at the highest rate possible for short intervals, triggered by ambient, local conditions) by the THEMIS spacecraft now open up the possibility of high-quality studies of EMIC waves, their growth, their saturation and their effects on particles.

[5] Presented here is a unique observation of a class of EMIC waves just below, at and through f_{He+}. These observations enable the first detailed examination of the observed plasma conditions giving rise to waves within the cold plasma He^+ stop band, and comparison with linear warm plasma theory. Although signatures of cold He^+ are clear in initial observations of the ion distributions, it is demonstrated that due to the combination of hot proton anisotropy and low density and nonzero temperature of the cold He^+ component, EMIC wave instability can occur within the frequency band that usually corresponds to the He^+ stop band under the cold plasma approximation. Our modeling results support the observations and further elucidate the range of cold ion densities and temperatures that support unstable EMIC waves without a heavy ion stop band and additional wave instabilities associated with warm plasma effects.

2. Instrumentation and Data Products

[6] The observations discussed within this study draw on various data products from the THEMIS mission [*Angelopoulos*, 2008]. The magnetic field data all originate from the fluxgate magnetometer (FGM) [*Auster et al.*, 2008]; spin-averaged (0.33 Samples/s) and low-resolution (4 Samples/s) FGM data types are used. The low-resolution magnetometer data provides three-dimensions of the ambient magnetic field from DC to 2 Hz Nyquist frequency. Details about the wave spectral analysis, including the transform methods used to produce the wave dynamic power spectrograms, are given in the section describing wave observations. Three-dimensional particle data measured by the electrostatic analyzer (ESA) [*McFadden et al.*, 2008] are also used. The spacecraft potential-derived plasma density (Ne_SCpot) data originated from measurements made by the electric field instrument (EFI) [*Bonnell et al.*, 2008]. Only data from THEMIS probe A (TH-A) are presented in this study.

3. Observations

[7] During the interval of interest TH-A was in the pre-midnight sector at a radial distance near geosynchronous altitude. To establish the background magnetic field that is used to define the field-aligned coordinate (FAC) system, the spin-averaged FGM data is low-pass filtered using a 600-point (30 min) sliding window. The low-resolution FGM data (4 S/s) is then transformed into the FAC system (Z along the average field, X perpendicular to Z in the direction of Earth and Y completing the orthogonal system) prior to performing any spectral analysis. The various types of ESA data are also transformed into and presented in FAC when applicable. Any additional data processing is described further in its respective section.

3.1. Waves

[8] EMIC wave observations made by TH-A during the time interval from 10:49:30 to 11:10:30 UT are summarized in Figure 1 in a stack plot showing the wave dynamic power spectrograms along the average magnetic field (plotted as magnetic field power spectral density along Z as defined in the FAC system and labeled P_z, with units of nT^2/Hz) produced using both fast Fourier (Figure 1a) and Morlet wavelet transform (Figure 1b) methods; degree of polarization (P^2) (Figure 1c); wave normal angle (θ) (Figure 1d); ellipticity (e) (Figure 1e); ESA ion (Ni_ESA), ESA electron (Ne_ESA) and spacecraft potential-derived (Ne_SCpot) densities (Figure 1f); and the computed DC magnetic field (Figure 1g). Local f_{H+} and f_{He+} are also superposed on each of the panels. The dynamic spectrogram produced via the fast Fourier transform (FFT) method in Figure 1a uses an FFT window of 256 points and a slide time of 128 points. Figures 1c–1e are products of the spectral matrix produced using the FFT method. Dynamic spectrograms produced using both FFT and Morlet wavelet transform (MWT) methods suggest that either one can be used for wave spectral analysis in this case; the results will remain similar.

[9] Wave spectral analysis and characterization draws upon procedures defined by *Samson and Olson* [1980]. The procedures include calculation of the wave degree of polarization, where $P^2 > 0.70$ indicates a high polarized wave, wave normal angle (θ) and ellipticity (e), which describe the wave's propagation angle with respect to B and the rotation sense of its perturbation vector, respectively. Values for θ range from 0 to $\pi/2$, for which a wave with $\theta = 0$ propagates purely parallel to the field and a wave with $\theta = \pi/2$ propagates perpendicular to the field. Values for e range between -1 to $+1$, where $e \approx -1$ indicates a left-hand polarized wave, $e = 0$ indicates linear polarization and $e \approx +1$ indicates a right-hand polarized wave. Moderate masking (using the NaN flag) is applied to the spectral analysis results to facilitate

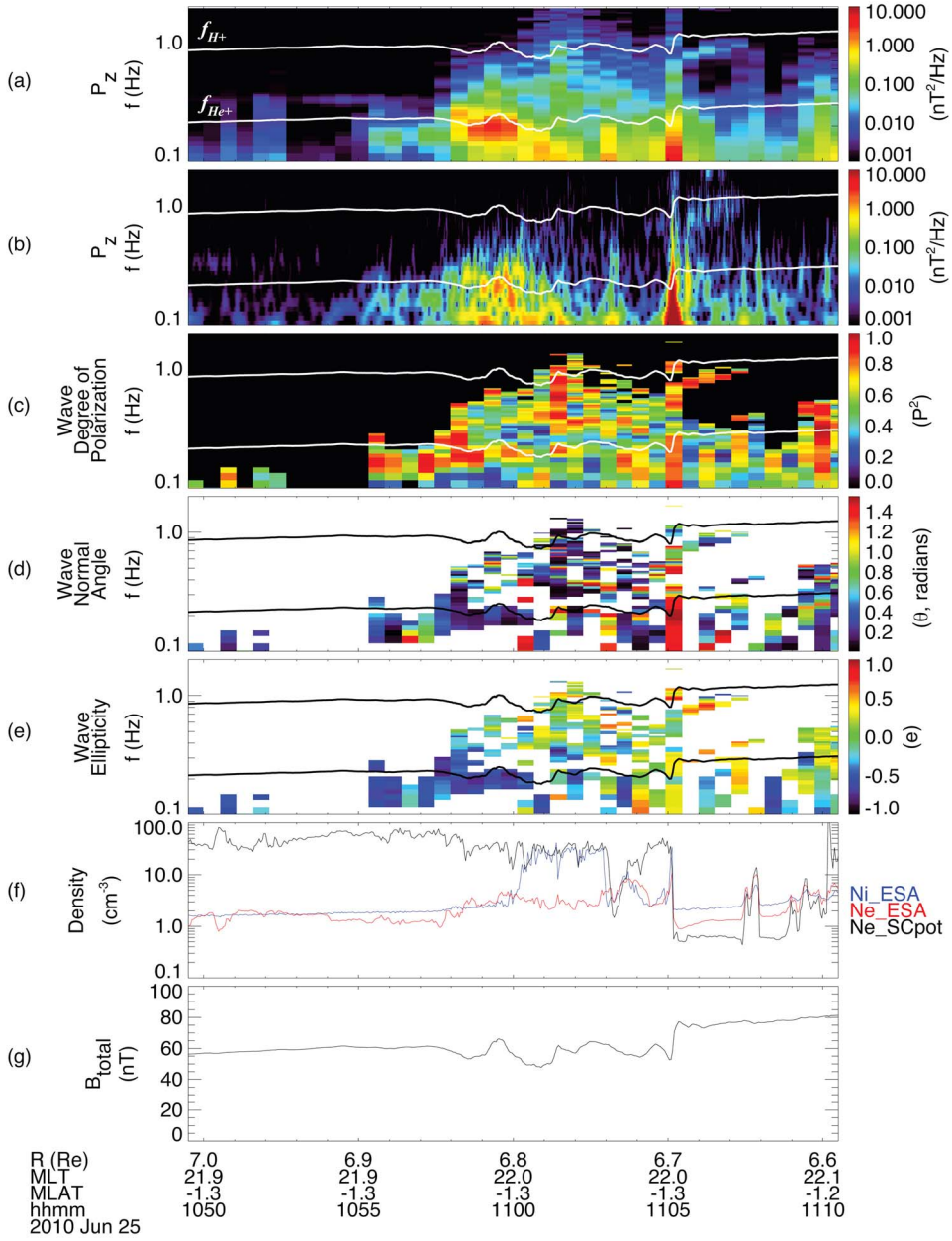

Figure 1. Stack plot summarizing the wave observations, spectral analysis results, approximate plasma densities and the computed background magnetic field.

interpretation: cells with wave power <0.01 nT^2/Hz are masked when plotting P^2, and cells with $P^2 < 0.5$ are masked when plotting θ and e. The masking eliminates much of the remaining spacecraft spin tones or harmonics from the plots and clears away some, though not all of the extraneous measurement noise.

[10] Wave observations can be partially characterized using the aforementioned spectral analysis tools. Between 10:55 and 11:02 UT, a series of peaks in wave power between 1 and 10 nT^2/Hz close to f_{He+} are visible in both Figure 1a and Figure 1b. It should also be noted that signatures of a magnetic field dipolarization are observed at about 11:05 UT, visible in Figure 1g as well as the accompanying panels. Within the interval prior to the dipolarization, which is the interval of interest in this paper, there are two smaller intervals from 10:57:50 to 10:58:40 UT and 11:00 to 11:01 UT when wave power along B_z is significant, coherent and present right below and across f_{He+} without a clear cold plasma stop band. We focus our attention on the waves during these two short intervals. It is clear that the highly polarized waves are propagating primarily parallel to the field ($\theta \approx 0$) and have left-handed rotation ($e < 0$), both attributes matching those of EMIC waves. However, since the waves are unstable both below and above f_{He+} the question arises whether the waves can be characterized as He^+ band waves, proton band waves, or both, strictly in the context of cold plasma theory. (It should be noted that the selected FFT spectral resolution is 0.002 Hz and frequency

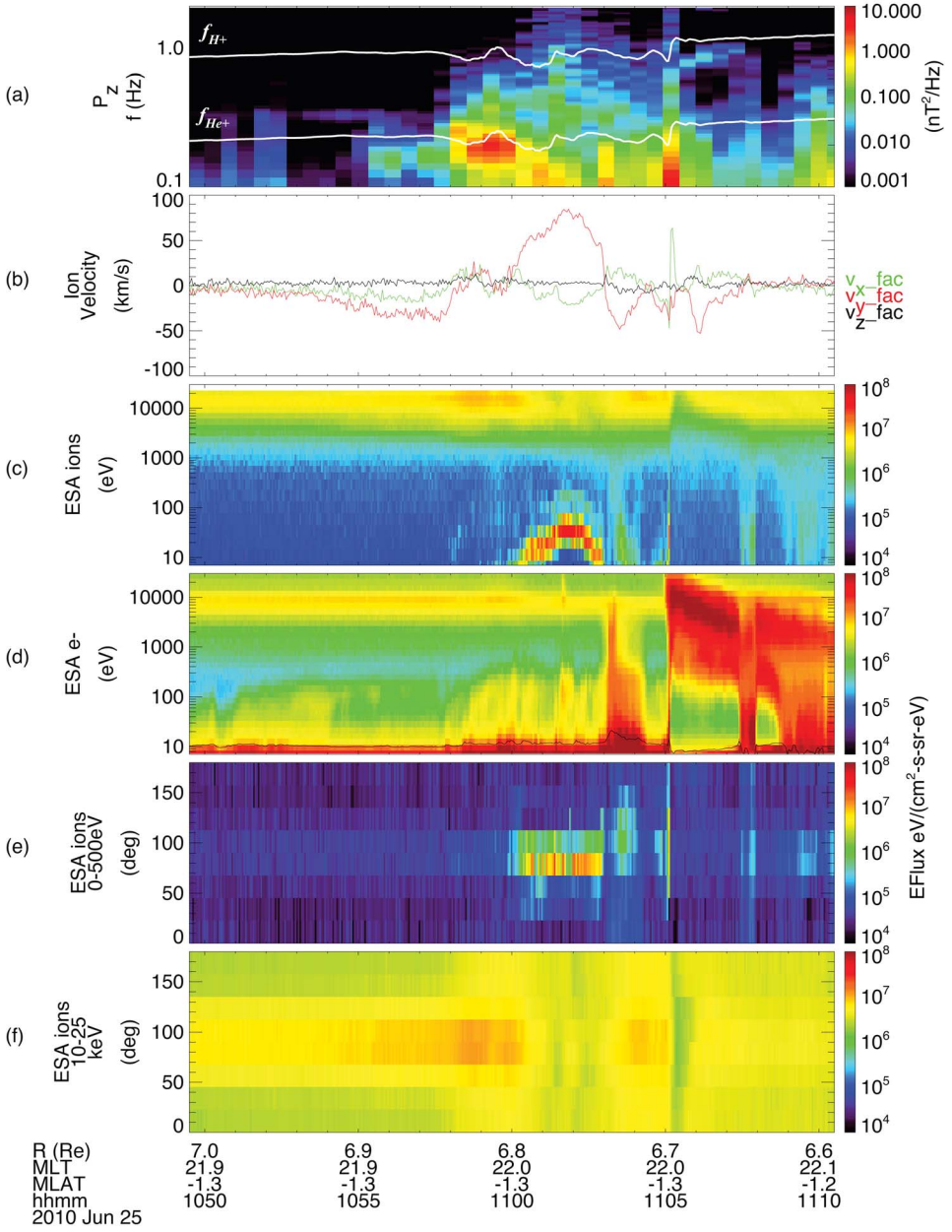

Figure 2. Stack plot summarizing the ESA observations during the interval of wave activity.

averaging has been avoided in order to avoid wave power overlap.)

[11] While in the cold plasma approximation clear stop bands appear near each heavy ion gyrofrequency and left-hand polarized waves cannot exist within the stop bands, the approximation is an oversimplification. To better address this concern, we consult observations of the plasma and particles and show that the waves indeed should exhibit signatures that differ from the familiar cold plasma case.

[12] Before closing this section, however, we point out that the differences in ion (Ni_ESA) and electron (Ne_ESA) densities in Figure 1f are purely instrumental and have to do with the spacecraft positive charging that repels ions up to an energy comparable to the spacecraft potential, while electron densities suffer in part from photoelectrons (but can be avoided by a good measure of the spacecraft potential from the electric field instrument) and in part from cold ambient electrons that cannot be distinguished well from the photoelectrons at very low energies. The spacecraft potential-determined density (Ne_SCpot), however, is not affected by missing the cold populations and can thus approximate the total plasma density quite well. It is evident that Ne_SCpot agrees with Ni_ESA between 11:00–11:03UT whereas everywhere before that the ion ESA underestimates the total ion density. We will come back to this point later in the paper.

3.2. Particles

[13] Data from the ESA instrument during the EMIC wave event are shown in Figure 2 (the wave power spectrum is shown in Figure 2a for reference). The ESA instrument measures ions (energy per charge without mass discrimination) from ~6–7 eV up to 25 keV and electrons from ~6–7 eV to

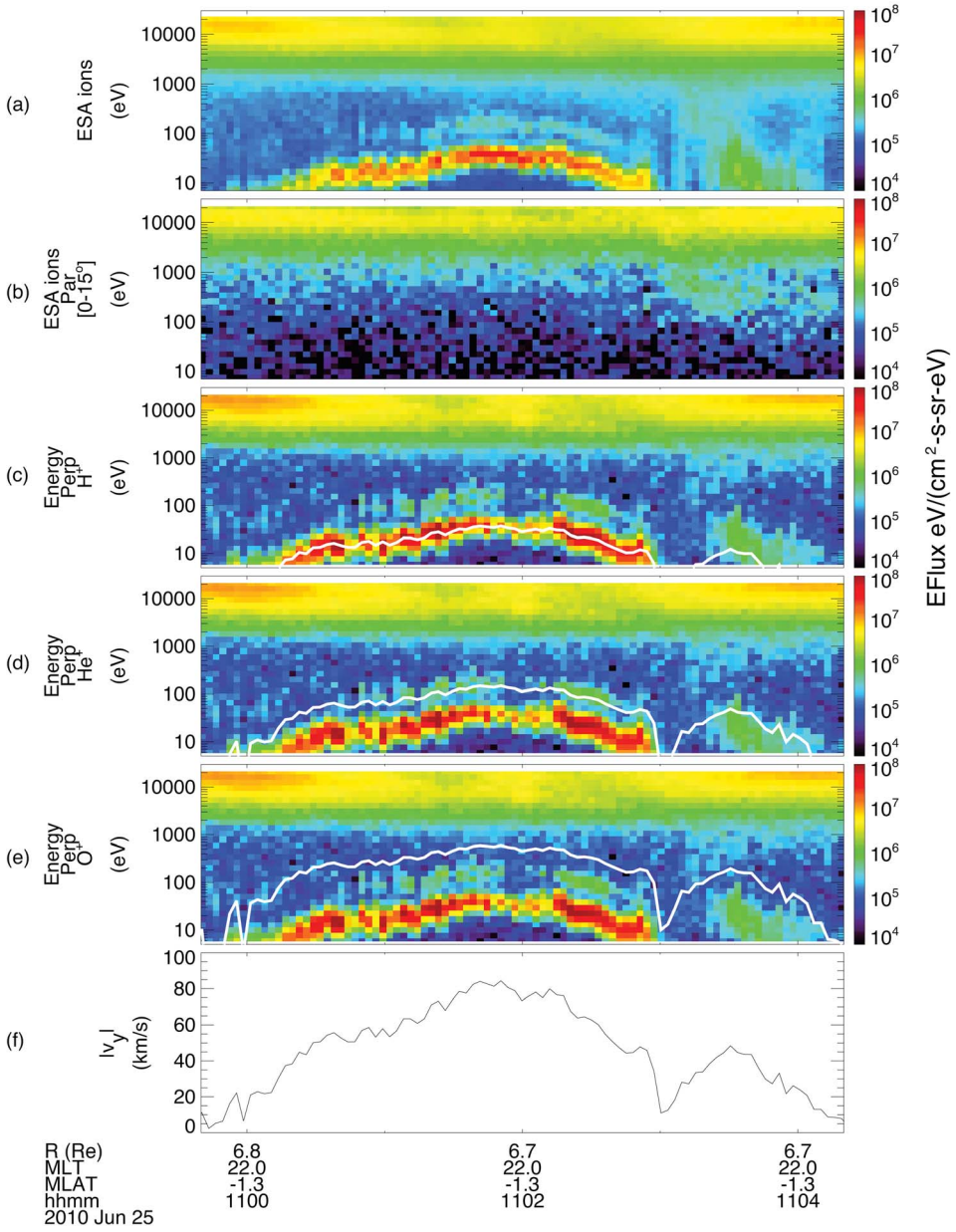

Figure 3. Stack plot showing the kinetic energy solutions of the cold ions detected during the fast plasma flow using $|v_y|$.

30 keV. Also shown are the ion flow velocities in the FAC system (Figure 2b), energy-time spectrograms for ions (Figure 2c) and electrons (Figure 2d), and two pitch angle spectrograms for energies: 5 to 500 eV (Figure 2e) and 10 to 25 keV (Figure 2f). Key features during the time interval appear from 10:58 to 11:00 UT and 11:00 to 11:03 UT.

[14] The time interval 10:58–11:00 UT corresponds to the period of maximum wave power. Looking at Figure 2f just before this interval, there is strong pitch angle anisotropy of the >10 keV ions (assumed protons), with more energy flux perpendicular to the background field. During this maximum wave power interval, the perpendicular energy flux intensifies but is also accompanied by enhanced energy flux parallel and anti-parallel to the field. We interpret the increase in parallel and anti-parallel energy flux as due to strong pitch angle scattering caused by cyclotron resonant scattering. The cyclotron resonant energy of energetic protons generally ranges from a few keV up to 10s of keV [e.g., *Gendrin and Roux*, 1980; *Chen et al.*, 2010], which agrees well with the observations.

[15] The second time interval, 11:00–11:03 UT, displays less wave power, but shows the onset of a fast plasma flow in Figure 2b, in v_y, peaking at about 80 km/s just before 11:02 UT. This flow also coincides in the ESA ion spectra, Figure 2c, as two energy flux peaks at energies less than 200 eV. The flow is also evidenced as flow anisotropy of low energy ions in Figure 2e as an energy flux concentrated perpendicular to the field. The pitch angle distribution of energetic ions shown in Figure 2f isotropizes during this interval of fast flow. The double peak in the energy flux

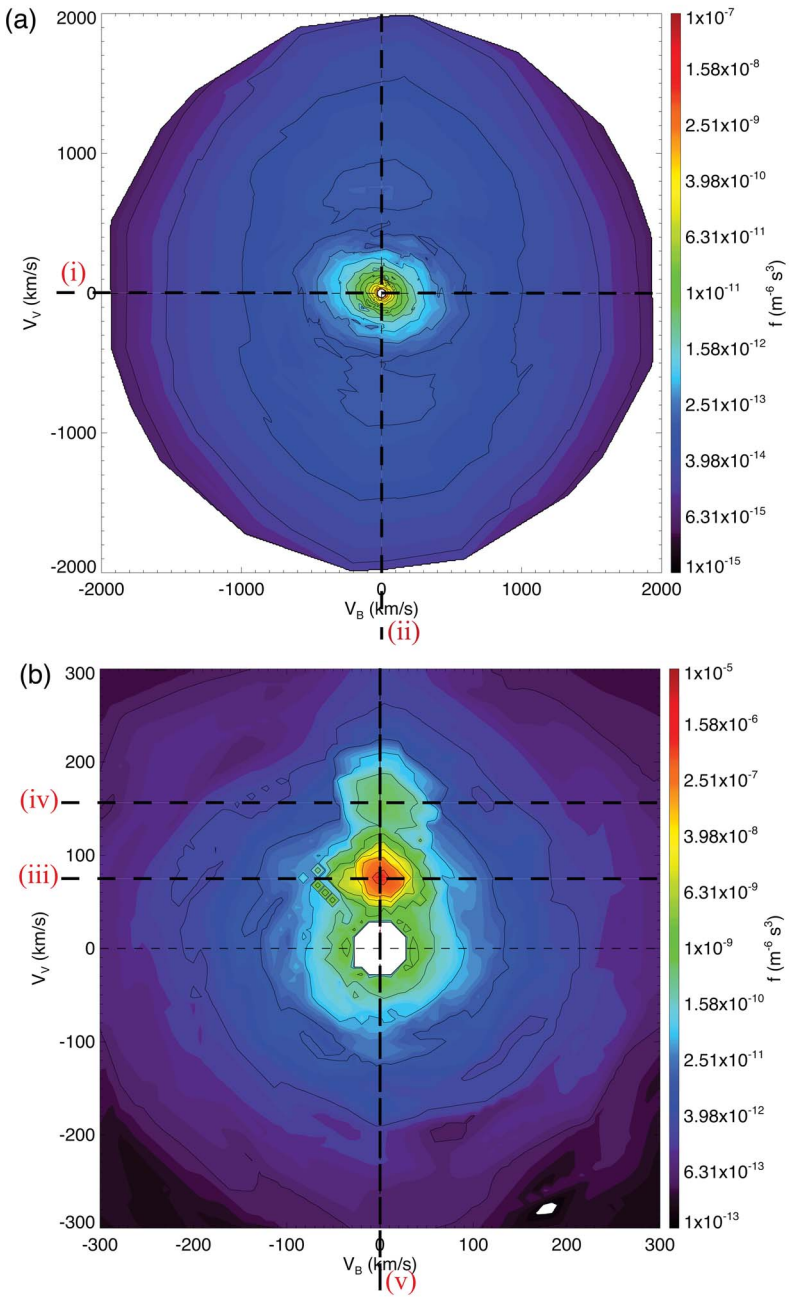

Figure 4. Observed phase space densities of (a) the full ion distribution function over the time interval 10:58:26–10:58:44 UT and (b) cold ions below 500 eV over the time interval 11:02:01–11:02:19 UT. The anisotropic energetic ions with velocities greater than 800 km/s in Figure 4a are assumed protons. The cold ions present within the fast plasma flow, indicated by the long horizontal dashed lines, are (iii) protons and (iv) He^+ and are re-plotted separately in Figure 5; the long vertical dashed line (v) denotes the cut along the perpendicular direction.

enhancement visible in Figure 2c between 11:00 and 11:03 UT requires additional explanation.

[16] As mentioned before, the ESA does not measure plasma composition. However, a straightforward calculation using the observed $|v_y|$ and proton, He^+ and O^+ masses allows the prediction of the ion kinetic energies if present during the fast flow. Cold protons carried by a fast flow of 80 km/s have a kinetic energy of $(0.5m_pv^2) \sim 30$ eV, while He^+ will have an energy $(0.5m_{He^+}v^2 = 2m_pv^2)$ of 120 eV. Figure 3 shows a zoomed interval from 10:59:40 to 11:04:20 UT when the ESA also recorded particle burst-mode data. The white traces superposed on Figures 3c, 3d and 3e are the kinetic energy solutions for protons, He^+ and O^+ if present during the fast flow. With the exception of Figure 3e, the traces match the detected ion energy peaks closely thus implying the presence of cold protons and He^+ in

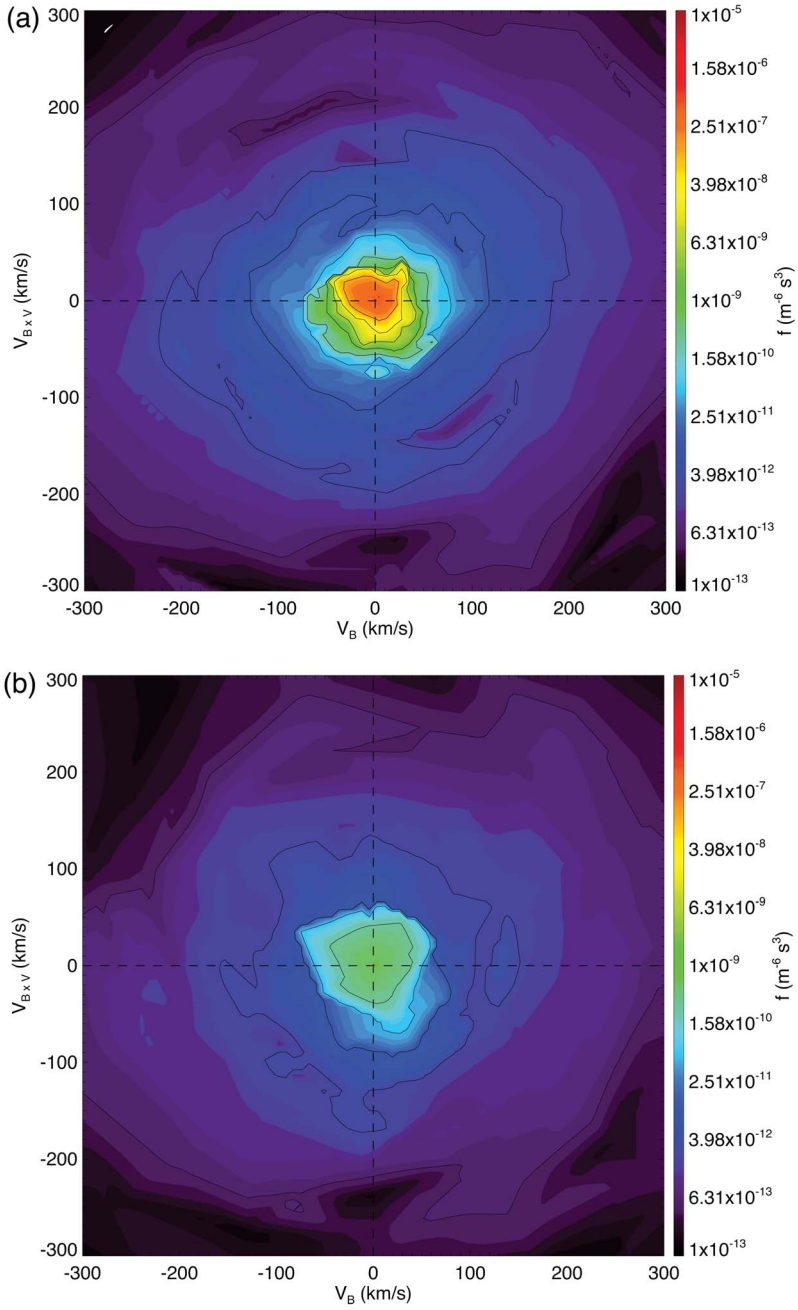

Figure 5. Observed phase space densities of the cold ions with the velocity space origins shifted using the offsets shown by the long horizontal dashed lines at (iii) 85 km/s and (iv) 155 km/s in Figure 4 over the time interval from 11:02:01 to 11:02:19 UT: (a) cold protons and (b) cold He^+.

significant densities. Any notable densities of O^+ would result in an additional peak above that of He^+; we therefore conclude that the plasma does not contain much O^+ at this time.

[17] At this point, recall that in Figure 1f the spacecraft potential-determined density, Ne_SCpot, agreed quite well with the ESA ion density, Ni_ESA, during the 11:00–11:03 UT interval, precisely the time when the low energy ions were measureable by the ESA instrument due to their flow velocity that enabled their energy to exceed the electrostatic repulsion from the positively charged spacecraft. This suggests that Ne_SCpot is a good measure of the plasma density. However, the fact that Ne_SCpot was actually larger than the ESA-determined density from both ions and electrons, and had a relatively large range from 20 to 80 cm^{-3} around the time of the wave activity suggests that the dominant part of the plasma is missed by the ESA instrument prior to the flow interval, and therefore primarily consists of cold plasma with energy below the sum of the spacecraft potential and the minimum ESA energy, i.e., $<\sim 11 + \sim 7 = \sim 18$ eV at 10:59 UT. The spacecraft potential has been superposed on the electron energy-time spectrogram (Figure 2d) as a solid black line.

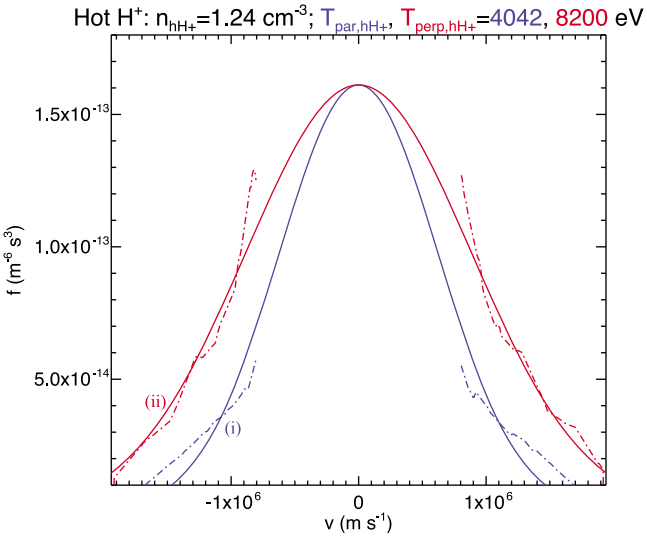

Figure 6. Bi-Maxwellian distribution (blue and red solid lines) fitted to the observed PSD cross-sections (blue and red dash-dotted lines) of hot protons shown by the dashed lines in Figure 4 (i) along the field, plotted in blue, and (ii) perpendicular to the field, plotted in red. The bi-Maxwellian distribution is fitted to the observed PSD of protons with energies greater than about 3 keV (800 km/s).

[18] The realization that multiple plasma species exist during the wave activity encourages a determination of the characteristics of each species by examining their observed phase space densities (PSD) to derive partial densities and temperatures. In Figure 4, 2D cuts of the observed three-dimensional ion distribution functions, averaged over an 18-s time interval, are shown in the B-V coordinate system, where B is along the magnetic field direction and V contains the average velocity vector during the interval. Specifically, Figure 4a shows the hot proton anisotropy from 10:58:26–10:58:44 UT, i.e., when the peak wave growth was seen, and Figure 4b shows the two cold ion energy flux enhancements from 11:02:01–11:02:19 UT. While it would have been ideal that the PSD contours are calculated over the same time interval, the cold ions were not in motion during the time of strong pitch angle anisotropy of the hot protons and eluded measurement by the ESA; it is assumed based on inference from the earlier discussion regarding Ne_SCpot that the cold ion distributions were also present during the interval of hot proton anisotropy. It is evident in Figure 4a that the hot protons are anisotropic, with more PSD distributed perpendicular (V_V) to the field than along (V_B) it. We mark the two directions (parallel and perpendicular) with lines (i) and (ii) to remind the reader that we will perform 1D cuts of this distribution along these lines later, for modeling. By comparison to the hot ions, the cold ions seen in Figure 4b are isotropic. The PSD of the cold ions can be analyzed separately by obtaining 2D velocity space cuts along the plane normal to the B-V plane that contain the dashed lines (iii) for cold protons, at 85 km/s, and (iv) for cold He^+, at 155 km/s. Additionally, the perpendicular cut for both ions is denoted by a vertical dashed line (v). The PSD is then recalculated for each cold ion distribution. In Figure 5, the individual PSD of cold protons (Figure 5a) and He^+ (Figure 5b) are shown, representing planar cuts intersecting the B-V plane along lines (iii) and (iv) in Figure 4.

[19] To obtain the density and temperature of each ion species, we fit the observed PSD to Maxwellian distributions. This is achieved using a least squares fit method. A single bi-Maxwellian distribution is used for fitting of the hot proton distribution due to the clear temperature anisotropy that was seen in Figure 4a. It should be noted that fitting of the anisotropic hot protons is achieved by excluding the PSD of ions with kinetic energies less than about 3 keV (800 km/s), which are seen to peak near the origin in Figure 4a. This kinetic energy cut-off was determined by considering that hot protons from a few keV to 10s of keV make up the expected resonant particle distribution. Fits with this kinetic energy cut-off shifted to ~2 and ~5 keV (600 and 1000 km/s, respectively) were also performed and yielded similar fitting results that also indicated clear temperature anisotropy of the hot proton distribution. However, we use the 3-keV energy cut-off to avoid including cooler particles in the fitting and to ensure that the fitting captures the previously noted energy range of resonant particles. The hot proton anisotropy, $A_{hH+} = T_{perp,hH+}/T_{par,hH+} - 1$, where $T_{perp,hH+}$ and $T_{par,hH+}$ are the perpendicular and parallel temperature of the hot protons, was about 1.03 for the fitting that excluded PSD of ions <3 keV (Figure 6). On the other hand, the roughly isotropic cold proton and He^+ distributions are fitted with Maxwellian distributions, as shown in Figures 7a and 7b. The densities and thermal characteristics of each ion species as obtained through the fitting are summarized in Table 1, along with other relevant parameters that help define the plasma environment during the interval of wave observations. The drift velocities are set to zero during the fitting of the various Maxwellian distributions to the PSD data.

4. Modeling

[20] The dispersion relation for parallel propagating EMIC waves and the various cases presented in this section follow the methodology described by *Chen et al.* [2011]; products are obtained using the wave dispersion relation in dimensionless form (following *Swanson* [1989]) and incorporate the plasma dispersion function as defined by *Fried and Conte* [1961]. The dispersion relation using the observed plasma parameters indeed demonstrates the presence of an unstable wave mode that can propagate across Ω_{He+}. Our results extend previously explored conditions for the unstable wave mode to very low-densities of the thermal He^+ plasma component (where "thermal" indicates ~1 eV < T_{He+} < 100 eV to distinguish He^+ from a typical cold plasma of $T \approx 1$ eV). To better understand the effects thermal He^+ density and temperature have on the propagation of the unstable wave mode, that component's density and temperature are alternately varied. Additionally, results of parametric study of the relationship of thermal He^+ characteristics to EMIC wave instability due to warm plasma effects are presented.

4.1. Dispersion Relation Using Observed Plasma Parameters

[21] The dispersion relation for parallel-propagating EMIC waves is shown in Figures 8a and 8b showing the real (ω_r) and imaginary (ω_i) wave frequencies (normalized to the proton gyrofrequency, Ω_{H+}) as a function of normalized wave

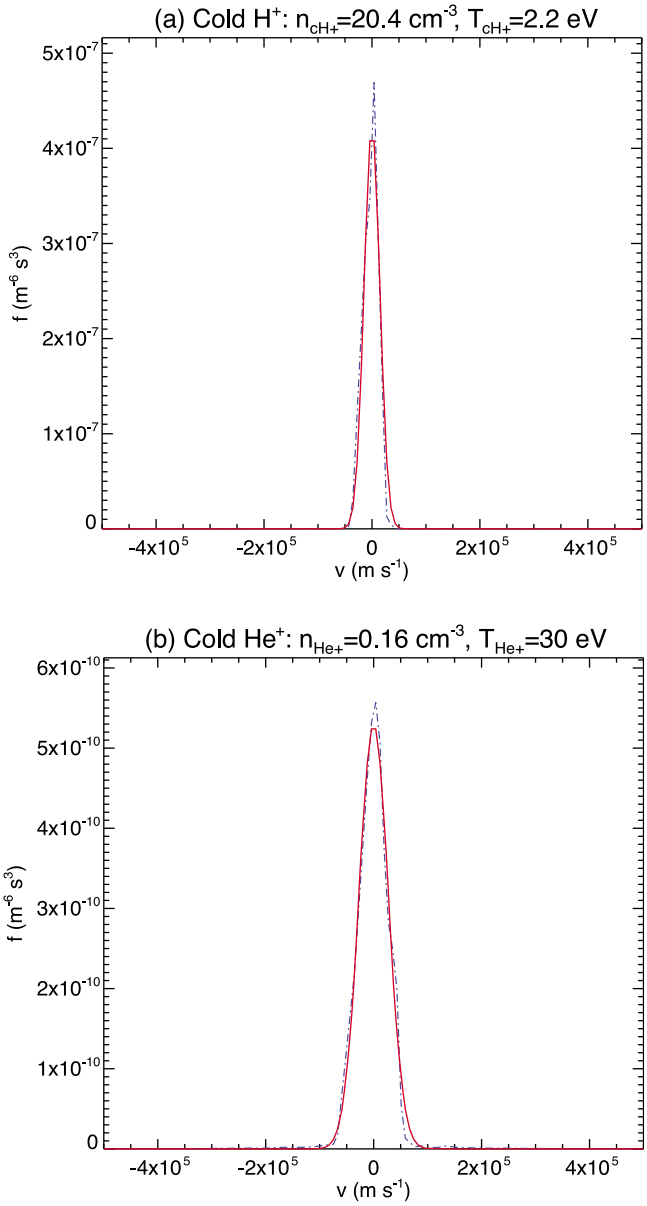

Figure 7. Maxwellian distributions (solid red lines) fitted to the PSD cross-sections (dash-dotted blue lines) of (a) cold protons and (b) cold He^+ as shown in Figure 5. Both ion species are assumed isotropic.

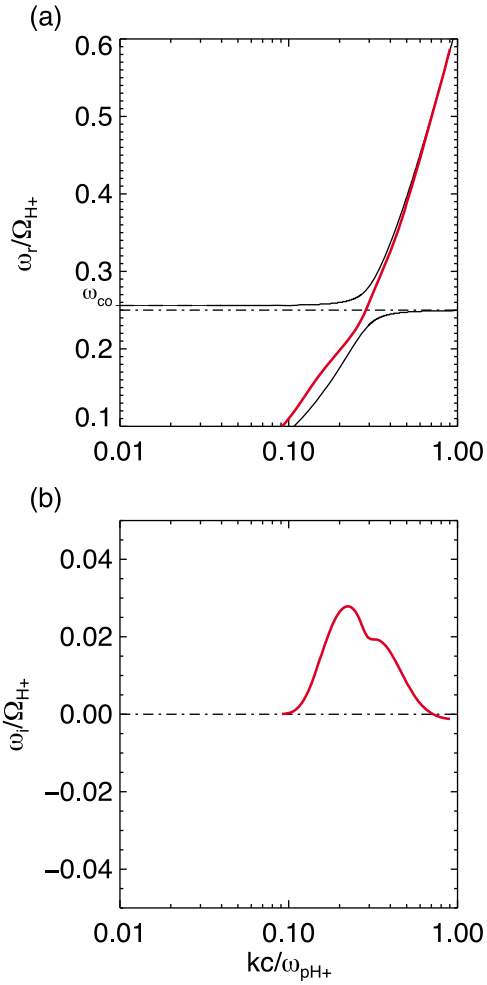

Figure 8. The dispersion relation for parallel propagating EMIC waves using the observed plasma parameters that shows (a) the relation between ω_r and k and (b) corresponding ω_i. Black horizontal dash-dotted lines in Figures 8a and 8b denote Ω_{He+} and $\omega_i = 0$, respectively. With all particle species' temperatures set to be cold and $n_{He+} = 0.16$ cm^{-3}, the cold plasma dispersion relation is plotted using thin black solid lines. The cut-off frequency, ω_{co}, is shown in Figure 8a with thin black dashed lines and labeled along the left vertical axis.

Table 1. A Summary of the Space Plasma Environment Parameters as Observed by TH-A on 25 June 2010[a]

Species	Hot Protons	Cold protons	Thermal He^+	Cold Electrons
n_s (cm^{-3})	1.24	20.4	0.16	21.8
$T_{par,s}$ (eV)	4042	2.2	30	1
$T_{perp,s}$ (eV)	8200	2.2	30	1

[a]The number densities and temperatures of the hot and cold protons and thermal He^+ are approximate values obtained from least squares fitting of Maxwellian distributions to the observed PSD. The cold electron component's density is based on the sum of all ion components and ensures charge neutrality. $B_o = 60$ nT; $n_{total} = 21.8$ cm^{-3}.

number, kc/ω_{pH+}, where c is the speed of light and ω_{pH+} is the plasma frequency of protons; ω_i is also referred to as the wave growth rate, where positive values correspond to wave growth. The results are consistent with our observations of maximum wave power detected very near f_{He+}. The dispersion relation is obtained in a homogeneous plasma containing cold electrons, cold protons with a Maxwellian distribution, thermal He^+ with a Maxwellian distribution and hot anisotropic protons with a bi-Maxwellian distribution. The thin black solid lines in Figure 8a show, for reference, the cold plasma dispersion relation, i.e., the case with $n_{He+} = 0.16$ cm^{-3} and all particle species temperatures set to be cold. The familiar banded structure is clear, with a narrow stop band starting at and ending just above Ω_{He+}, where the stop band is between Ω_{He+} and the cut-off frequency ($\Omega_{He+} < \omega_r < \omega_{co}$), labeled ω_{co} and denoted with a thin black dashed

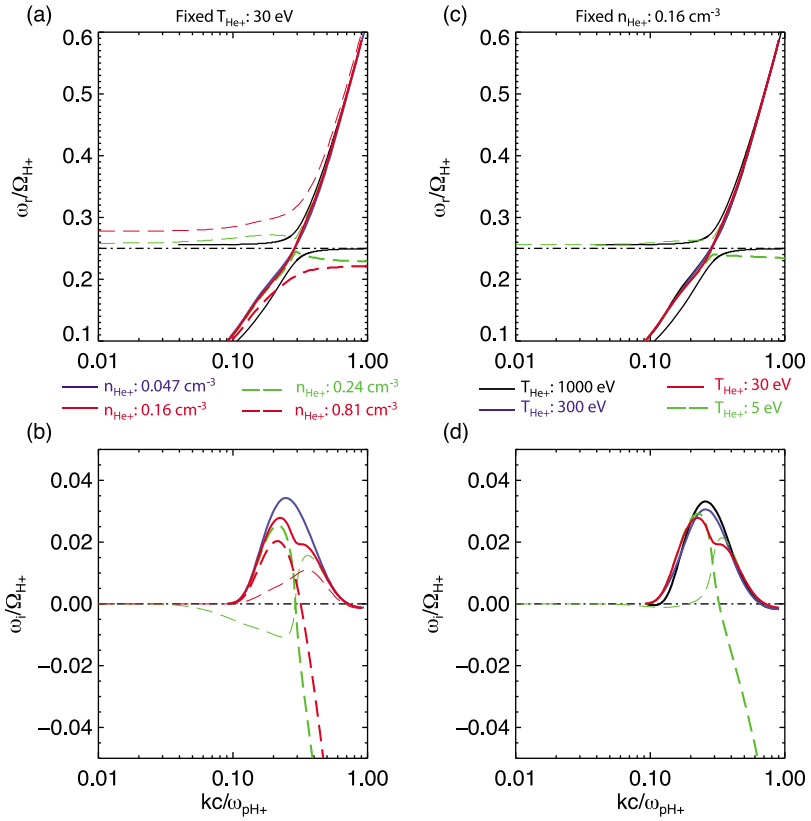

Figure 9. Several EMIC wave dispersion relation cases under Ω_{H+} obtained while varying He^+ density and temperature. (a) The relation between ω_r and k while varying thermal He^+ density at fixed temperature (T_{He+} = 30 eV) and (b) corresponding ω_i. (c) The relation between ω_r and k while varying He^+ temperature at fixed density (n_{He+} = 0.16 cm^{-3}) and (d) corresponding ω_i. Thin black dash-dotted horizontal lines in Figures 9a and 9b indicate Ω_{He+} and $\omega_i = 0$, respectively; again, thin black solid lines represent the cold plasma dispersion relation for n_{He+} = 0.16 cm^{-3} with all particle species' temperatures set to be cold. In Figures 9a–9d, long dashed lines represent the cases for which a He^+ stop band exists, where thick long dashed lines show ω_r and ω_i as a function of k for the He^+ band ($\omega_r < \Omega_{He+}$) and thin long dashed lines designate the relations for the proton band ($\Omega_{He+} < \omega_r < \Omega_{H+}$); thick solid lines represent the cases for no stop band, where thick red solid lines represent the observed case. Only the noted He^+ characteristics are varied; the remaining plasma parameters remain the same as the observed case, summarized in Table 1.

line. The thick red solid line in Figure 8a shows that the wave mode can indeed propagate across Ω_{He+}. It possesses maximum growth rate just under Ω_{He+} (Figure 8b), but has positive growth rates over a frequency range including Ω_{He+} as well as above it.

[22] It should be noted that the observed plasma parameters applied to the dispersion relation shed new light on previous results obtained by *Chen et al.* [2011]. In previous work, the unstable mode caused by the hot proton anisotropy ($n_{hH+} > 7.5\%$; $T_{par,hH+} > 25$ keV; $A_{hH+} > 1.3$) that propagates across Ω_{He+} is produced under the primary condition of sufficiently high He^+ temperature ($T_{He+} > 100$ eV) and lower density ($n_{He+} < 4\%$). The present study probes the low He^+ density condition at a He^+ temperature at least a factor of 3 lower than the previously presented nominal case. It is also shown here that the unstable mode also occurs in a high-density, cold plasma ($n_{total} \sim 20$ cm^{-3}; $\omega_{pe}/|\Omega_e| \sim 20$) with hot proton temperature anisotropy ($n_{hH+} \sim 5\%$; $T_{par,hH+} \sim 4$ keV; $A_{hH+} \sim 1$), but with very low densities of thermal He^+ ($n_{He+} < 1\%$; $T_{He+} \sim 30$ eV). The new results refine the low-density warm He^+ condition and show that the unstable mode occurs within plasma containing much cooler He^+ and that the instability threshold may be exceeded due to a combination of the heavy ion's density and minimum temperature. To explore the density dependence of the unstable mode, the He^+ density is varied while keeping all other parameters unchanged. Although *Chen et al.* [2011] have noted temperature variation of He^+ as having a smaller effect on the dispersion relation, He^+ temperature is also varied separately to compare alongside the effects of density variation.

4.2. Variation of Thermal He^+ Density and Temperature

[23] The role of thermal He^+ characteristics on the unstable wave mode that propagates through Ω_{He+} can be explored numerically to better understand the contribution of density and temperature to the wave mode's occurrence. The EMIC wave dispersion relation at different He^+ densities is presented in Figures 9a and 9b. The observed case is plotted using thick red solid lines. It is clear that as He^+ density increases above the observed value (long dashed lines), the

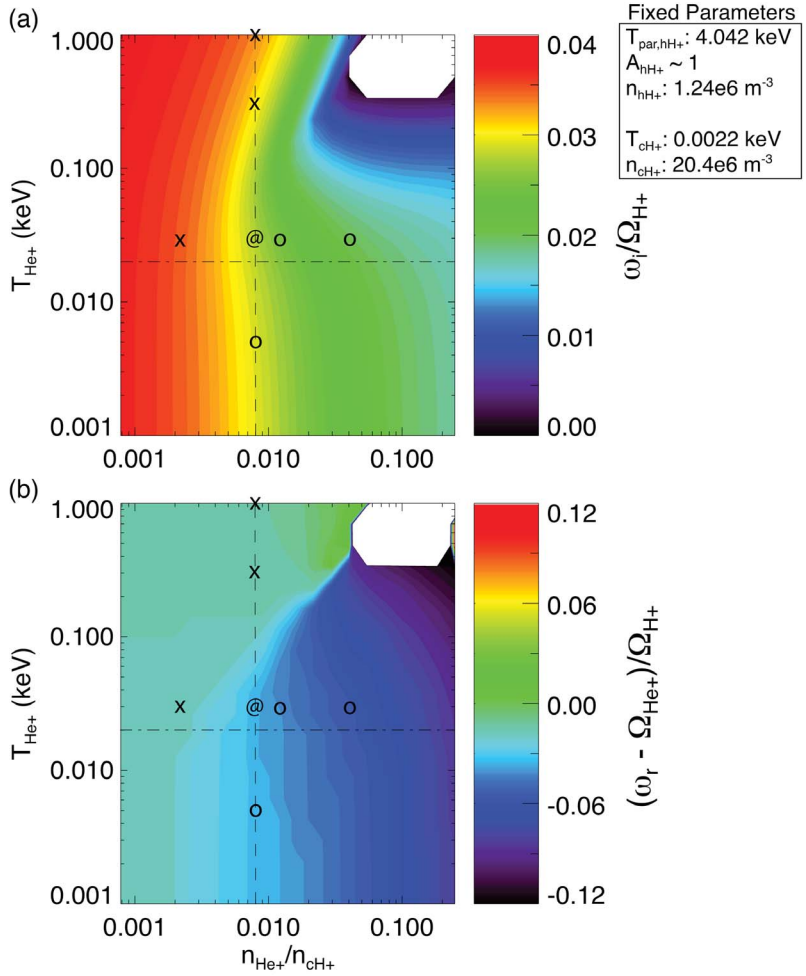

Figure 10. Contours of (a) peak ω_i and (b) ($\omega_r - \Omega_{He+}$) where peak growth rate occurs for 20 different n_{He+} at 20 different T_{He+}. Symbols @, x, and o designate the cases presented in Figure 9: @ indicates the observed case, "x" indicates the cases without a He^+ stop band, and "o" indicates the cases for which a He^+ stop band exists. Horizontal dash-dotted lines designate T_{He+} = 0.02 keV and vertical dashed lines designate n_{He+}/n_{cH+} = 0.008 (n_{He+} = 0.16 cm^{-3}).

dispersion relation reverts back to resembling the cold plasma case. The stop band grows wider with elevated He^+ density, as more He^+ is available to damp the waves. This process of wave damping and subsequent He^+ heating has received much attention in the past [*Young et al.*, 1981]. It should also be noted that in the cases in which the wave modes split into two frequency bands, the waves have larger growth rates at wave frequencies below Ω_{He+}.

[24] He^+ temperature variations indeed also affect the occurrence and propagation of the unstable mode, as previously noted. Traces of the dispersion relation at different He^+ temperatures are presented in Figures 9c and 9d for fixed density. It is apparent that if the He^+ temperature drops below 5 eV (green dashed lines), the dispersion relation splits into two separate modes, suggesting He^+ that has been heated even slightly (e.g., above 5 eV for $n_{He+} \sim 0.7\%$) can still play a role in generation of the unstable wave mode across the He^+ gyrofrequency. Even if the He^+ stop band appears again when He^+ temperature drops below the threshold for the single unstable EMIC wave mode, warm plasma effects continue to affect dispersion for wave numbers at ω_r near Ω_{He+}, specifically, catastrophic damping occurs at high wave numbers, which was previously noted by *Chen et al.* [2011] to place severe limits on the scattering energies of electrons. As He^+ temperature increases above the observed temperature to 300 eV (thick blue solid line) and 1000 eV (thick black solid line), the single unstable wave mode becomes more defined and the maximum growth rate increases; the range of wave frequencies with positive growth rate narrows slightly.

[25] In summary, we find that it is the combination of thermal He^+ density and temperature that contributes to the occurrence of the single unstable wave mode. Very low density of He^+ leads to increased instability and larger deviation from the cold plasma dispersion relation. Conversely, high He^+ component densities result in damping of EMIC waves with ω_r near Ω_{He+}. Although the observed temperature is lower than the nominal case presented by *Chen et al.* [2011], the temperature is still warmer than that of typical plasmaspheric cold ions of a few eV. The fact that an

extended temperature range leads to instability of a single, crossing mode suggests a possible mode evolution: cold heavy ions enable initial wave growth but it is not until moderate heating of those ions occurs that the waves can extend over a broad frequency range and resonate with an energy range of both hot ions and relativistic electrons that differs significantly from the cold plasma approximation.

4.3. Parametric Study of Thermal He^+ Effects on EMIC Wave Instability

[26] An extended study of the specific cases presented in Figure 9 is undertaken to obtain a larger picture of the relationship of thermal He^+ parameter variability to EMIC wave instability. A wide range of parameters are studied by varying twenty increments of n_{He+}/n_{cH+}, from 0.0008 to 0.25, at twenty increments of T_{He+}, from 0.001 to 1 keV; the remaining ion components' parameters remained fixed and the cold electron component density was varied only to maintain charge neutrality. The 400 cases are visualized in Figure 10 as two contour plots that show the peak ω_i for each case (Figure 10a) and $(\omega_r - \Omega_{He+})$ where the peak ω_i occurs (Figure 10b); cases with $\omega_i/\Omega_{H+} < 0.001$ are masked in both plots. The cases from Figure 9 are superposed as symbols on the contour plots.

[27] The contours of peak ω_i, Figure 10a, show a few trends. The density dependence of peak ω_i is immediately apparent: increasing n_{He+}/n_{cH+} at any T_{He+} results in decreasing peak ω_i; for $T_{He+} < 0.02$ keV, peak ω_i decreases monotonically with increasing n_{He+}/n_{cH+}; for $T_{He+} > 0.02$ keV, peak ω_i also decreases with increasing n_{He+}/n_{cH+} but evolves in a less organized manner, e.g., sudden drop-offs in peak ω_i occur for $T_{He+} > 0.1$ keV as n_{He+}/n_{cH+} increases above 0.02. Additional trends can be seen when examining for temperature influences on peak ω_i at a given n_{He+}/n_{cH+}: the first trend is present only at $n_{He+}/n_{cH+} < 0.002$, as increasing T_{He+} leads to increasing peak ω_i; an opposite trend is present at $n_{He+}/n_{cH+} > 0.05$, where increasing T_{He+} leads to decreasing peak ω_i; and, for $0.002 < n_{He+}/n_{cH+} < 0.05$, variations of T_{He+} can lead to both increasing and decreasing peak ω_i. An example of the last trend can be seen at $n_{He+}/n_{cH+} = 0.008$ and also in Figures 9c and 9d: as T_{He+} is increased incrementally from 0.001 to 1 keV, peak ω_i starts out near 0.03, decreases toward 0.02 and then increases toward 0.04.

[28] Additional trends surface when examining the value of $(\omega_r - \Omega_{He+})$ where peak ω_i occurs, Figure 10b. For any T_{He+}, increasing n_{He+}/n_{cH+} results in peak ω_i occurring at larger deviations from Ω_{He+} (i.e., $|\omega_r - \Omega_{He+}|$ increases). For $0.0008 < n_{He+}/n_{cH+} < 0.01$, increasing T_{He+} leads to decreasing $|\omega_r - \Omega_{He+}|$, with higher T_{He+} leading to peak ω_i occurring at ω_r very near Ω_{He+} (i.e., $(\omega_r - \Omega_{He+}) \sim 0$). For $n_{He+}/n_{cH+} > 0.01$, peak growth is confined to $(\omega_r - \Omega_{He+}) < 0$, even for increasing T_{He+}. Again, $T_{He+} \sim 0.02$ keV appears to be an important temperature. For $0.002 < n_{He+}/n_{cH+} < 0.05$, the temperature is seen to separate two distinct behaviors of the $(\omega_r - \Omega_{He+})$ contours; for $T_{He+} < 0.02$ keV, $(\omega_r - \Omega_{He+}) < 0$ and remains nearly the same at any given density; this changes significantly as heating to $T_{He+} > 0.02$ keV occurs, with $(\omega_r - \Omega_{He+}) \sim 0$ and eventually positive at higher temperatures.

[29] Results of the parametric study reemphasize significant points brought up in previous sections. We find that the effects of heavy ion characteristics in the presence of hot proton anisotropy on EMIC wave instability are strongly coupled to density changes but are also influenced by changes in temperature. In particular, the changes in peak ω_i and $(\omega_r - \Omega_{He+})$ as T_{He+} increases above 0.02 keV for $0.002 < n_{He+}/n_{cH+} < 0.05$ supports the suggestion in Section 4.2 of an EMIC wave mode evolution that occurs only when He^+ is heated above a critical temperature.

5. Discussion and Conclusions

[30] Although the observations and modeling results agree well, the clear signatures of wave power crossing over f_{He+} could have a different explanation, which we explore and refute here. The possibility exists that in the presence of parallel flows the waves are Doppler-shifted into the range of the local gyrofrequency. Close inspection of the ion velocity moments in Figure 2b shows that v_z also shows a small but finite flow velocity of a few km/s. The peak flows in v_z occur in the time interval 10:58–11:00 UT, coincident with the dominant wave power and signatures of f_{He+} crossover. However, the flows in v_z are exceedingly small and certainly <10 km/s. From the angular real frequency of the dispersion relation at peak power we obtain $\omega_r \approx 0.24$ rads/s, with $\Omega_{He+} = 0.25$ rads/s. From the dispersion relation, for $\omega_r = 0.24$ rads/s, $kc/\omega_{pH+} \approx 0.3$, which corresponds to $k = k_z = 5.265\text{e-}3$ km^{-1}. A plasma flow with $v_z = 10$ km/s may then cause a Doppler-shift $\Delta\omega_r \approx 0.0526$ rads/s, bringing the peak power waves through the local gyrofrequency and into the stop band. Larger or smaller gains in frequency can be observed for different speeds. While minor plasma flows in v_z can Doppler-shift f_{actual} closer to the He^+ stop band, the wave emissions observed from 11:00–11:01 UT, which also show wave power just under and through f_{He+}, cannot be explained in this way. Moreover, flows on the order of a few km/s are very near the random noise value of the ESA instrument (and consistent with statistical fluctuations of the hot plasma thermal velocity of several 100s of km/s). We therefore suggest that while this possibility of a Doppler-shift is not out of the question, it is not the most likely explanation of the observed, persistent presence of wave power within the He^+ stop band.

[31] We would also like to point out that the technique we have used to determine the plasma composition during the EMIC wave observations could be applied toward future cases. As discussed earlier, the positive spacecraft potential repels the majority of the ambient cold ions under steady conditions. However, flows associated with ULF waves and convection are commonplace throughout the magnetosphere and may allow sampling of these cold ion populations. Some preliminary limits for use of this plasma composition technique have been determined using the observed spacecraft potential and ion flow velocities. In the absence of flows ($v = 0$) and a spacecraft potential <12 V (+ ~7 eV ion ESA minimum energy), protons with thermal velocities $v_{th} = (k_B T/m_p)^{-1/2} \approx 41.5$ km/s or larger ($T_{H+} > 18$ eV) can be sampled. A flow velocity >60 km/s ($0.5 m_p v^2 \sim 19$ eV) at 11:02 UT allowed for clear sampling of the cold proton species ($T_{H+} \sim 2.2$ eV); the spacecraft potential was near 11 V at this time such that protons with energies >11 + ~7 eV = 18 eV were within the minimum energy threshold and could be discerned by the ion ESA. This suggests that for

flow velocities >60 km/s and a spacecraft potential <12 V, even 0 eV particles may be sampled by the ion ESA. The limits for sampling of the additional heavy ion species He^+ and O^+ can be determined using the straightforward methodology discussed above. Conditions matching these initial limits are easily satisfied throughout the magnetosphere, allowing for the application of this technique toward determining the composition of the equatorial magnetosphere as well as clarifying the conditions for EMIC wave growth.

[32] In summary, a unique observation of EMIC waves by TH-A has been presented in this paper. Fortuitous observations of the cold ions that were likely present throughout the period of wave growth were made by taking advantage of an enhanced flow period just shortly after the peak EMIC wave power was observed. Using a numerical solution of the linear warm plasma dispersion relation we found that the unstable EMIC wave mode obtained from parameters consistent with observations has maximum growth rate just below Ω_{He+}, is unstable from below Ω_{He+} and without a stop band at Ω_{He+} and thus does not fit the typical characteristics of the cold plasma dispersion relation. The results provide the first observational evidence of a class of EMIC waves predicted by warm plasma theory that can be unstable within a cold plasma stop band. As recent theoretical work has already shown, EMIC waves that do not have a cold plasma stop band(s) are severely damped at higher wave number and, thus, can only interact with high-energy electrons > a few MeV. It remains to be determined experimentally where this class of EMIC waves occurs and the conditions of the plasma environment that support their genesis. If these waves are a common occurrence, their existence will significantly alter predictions of their influence on high-energy electron scattering.

[33] Parametric study of the density and temperature of thermal He^+ further illustrated the competition between various ion plasma species and the influences of the heavy ion's characteristics on EMIC wave instability, reiterating the importance of considering individual ions' attributes to more accurately characterize EMIC waves. The realization that a multispecies plasma containing low densities of thermal He^+ can engender EMIC waves that are not damped at the heavy ion's gyrofrequency has implications for theories seeking to quantify the effects the waves have on related processes, such as ion heating and losses of high-energy electrons. Investigation of additional wave and particle observations can provide more accurate maps of heavy ion density and temperature in the magnetosphere and the corresponding effects on EMIC waves, even when cold plasma and composition measurements are impossible or hard to make.

[34] **Acknowledgments.** The authors acknowledge NASA THEMIS contract NAS5-02099 and the THEMIS team. Specifically: C. W. Carlson and J. P. McFadden for use of the ESA data; J. W. Bonnell and F. S. Mozer for use of EFI data; and K. H. Glassmeier, U. Auster and W. Baumjohann for the use of FGM data provided under the lead of the Technical University of Braunschweig and with financial support through the German Ministry for Economy and Technology and the German Center for Aviation and Space (DLR) under contract 50 OC 0302.

[35] Robert Lysak thanks the reviewers for their assistance in evaluating this paper.

References

Angelopoulos, V. (2008), The THEMIS Mission, *Space Sci. Rev.*, *141*, 5–34, doi:10.1007/s11214-008-9336-1.

Auster, H. U., et al. (2008), The THEMIS Fluxgate Magnetometer, *Space Sci. Rev.*, *141*, 235–264, doi:10.1007/s11214-008-9365-9.

Bonnell, J. W., et al. (2008), The Electric Field Instrument (EFI) for THEMIS, *Space Sci. Rev.*, *141*, 303–341, doi:10.1007/s11214-008-9469-2.

Chen, L., R. M. Thorne, and R. B. Horne (2009), Simulation of EMIC wave excitation in a model magnetosphere including structured high-density plumes, *J. Geophys. Res.*, *114*, A07221, doi:10.1029/2009JA014204.

Chen, L., R. M. Thorne, V. K. Jordanova, C.-P. Wang, M. Gkioulidou, L. Lyons, and R. B. Horne (2010), Global simulation of EMIC wave excitation during the 21 April 2001 storm from coupled RCM-RAM-HOTRAY modeling, *J. Geophys. Res.*, *115*, A07209, doi:10.1029/2009JA015075.

Chen, L., R. M. Thorne, and J. Bortnik (2011), The controlling effect of ion temperature on EMIC wave excitation and scattering, *Geophys. Res. Lett.*, *38*, L16109, doi:10.1029/2011GL048653.

Fraser, B. J., R. S. Grew, S. K. Morley, J. C. Green, H. J. Singer, T. M. Loto'aniu, and M. F. Thomsen (2010), Storm time observations of electromagnetic ion cyclotron waves at geosynchronous orbit: GOES results, *J. Geophys. Res.*, *115*, A05208, doi:10.1029/2009JA014516.

Fried, B. D., and S. D. Conte (1961), *The Plasma Dispersion Function*, Academic, New York.

Gendrin, R., and A. Roux (1980), Energization of helium ions by proton-induced hydromagnetic waves, *J. Geophys. Res.*, *85*(A9), 4577–4586, doi:10.1029/JA085iA09p04577.

Li, W., et al. (2010), THEMIS analysis of observed equatorial electron distributions responsible for the chorus excitation, *J. Geophys. Res.*, *115*, A00F11, doi:10.1029/2009JA014845.

Mauk, B. H., and R. L. McPherron (1980), An experimental test of the electro-magnetic ion cyclotron instability within the earth's magnetosphere, *Phys. Fluids*, *23*, 2111, doi:10.1063/1.862873.

McFadden, J. P., et al. (2008), The THEMIS ESA plasma instrument and in-flight calibration, *Space Sci. Rev.*, *141*, 277–302, doi:10.1007/s11214-008-9440-2.

Meredith, N. P., R. M. Thorne, R. B. Horne, D. Summers, B. J. Fraser, and R. R. Anderson (2003), Statistical analysis of relativistic electron energies for cyclotron resonance with EMIC waves observed on CRRES, *J. Geophys. Res.*, *108*(A6), 1250, doi:10.1029/2002JA009700.

Roux, A., S. Perraut, J. L. Rauch, C. de Villedary, G. Kremser, A. Korth, and D. T. Young (1982), Wave-particle interactions near Ω_{He+} observed on board GEOS 1 and 2: 2. Generation of ion cyclotron waves and heating of He^+ ions, *J. Geophys. Res.*, *87*, 8174–8190, doi:10.1029/JA087iA10p08174.

Samson, J. C., and J. V. Olson (1980), Some comments on the descriptions of the polarization states of waves, *Geophys. J. R. Astron. Soc.*, *61*, 115–129, doi:10.1111/j.1365-246X.1980.tb04308.x.

Shoji, M., and Y. Omura (2011), Simulation of electromagnetic ion cyclotron triggered emissions in the Earth's inner magnetosphere, *J. Geophys. Res.*, *116*, A05212, doi:10.1029/2010JA016351.

Shoji, M., Y. Omura, B. Grison, J. Pickett, I. Dandouras, and M. Engebretson (2011), Electromagnetic ion cyclotron waves in the helium branch induced by multiple electromagnetic ion cyclotron triggered emissions, *Geophys. Res. Lett.*, *38*, L17102, doi:10.1029/2011GL048427.

Silin, I., I. R. Mann, R. D. Sydora, D. Summers, and R. L. Mac (2011), Warm plasma effects on electromagnetic ion cyclotron wave MeV electron interactions in the magnetosphere, *J. Geophys. Res.*, *116*, A05215, doi:10.1029/2010JA016398.

Swanson, D. G. (1989), *Plasma Waves*, Academic, Boston, Mass., doi:10.1887/075030927X.

Thorne, R. M., and C. F. Kennel (1971), Relativistic electron precipitation during magnetic storm main phase, *J. Geophys. Res.*, *76*, 4446–4453, doi:10.1029/JA076i019p04446.

Ukhorskiy, A. Y., Y. Y. Shprits, B. J. Anderson, K. Takahashi, and R. M. Thorne (2010), Rapid scattering of radiation belt electrons by storm-time EMIC waves, *Geophys. Res. Lett.*, *37*, L09101, doi:10.1029/2010GL042906.

Usanova, M. E., I. R. Mann, I. J. Rae, Z. C. Kale, V. Angelopoulos, J. W. Bonnell, K.-H. Glassmeier, H. U. Auster, and H. J. Singer (2008), Multipoint observations of magnetospheric compression-related EMIC Pc1 waves by THEMIS and CARISMA, *Geophys. Res. Lett.*, *35*, L17S25, doi:10.1029/2008GL034458.

Young, D. T., S. Perraut, A. Roux, C. de Villedary, R. Gendrin, A. Korth, G. Kremser, and D. Jones (1981), Wave-particle interactions near Ω_{He+} observed on GEOS 1 and 2: 1. Propagation of ion cyclotron waves in He^+-rich plasma, *J. Geophys. Res.*, *86*, 6755–6772, doi:10.1029/JA086iA08p06755.